11th World Congress on Computational Mechanics (WCCM XI)
5th European Conference on Computational Mechanics (ECCM V)
6th European Conference on Computational Fluid Dynamics (ECFD VI)
E. Oñate, J. Oliver and A. Huerta (Eds)

# NUMERICAL INVESTIGATION OF AN AIRFOIL WITH SELF-ADAPTIVE CAMBER

**S. TÜRK[1,2], H. SPIEGELBERG[1], M. SCHÄFER[2], C. TROPEA[3] and D.C. STERNEL[2]**

[1] Graduate School of Computational Engineering, TU Darmstadt, Dolivostraße 15, 64293 Darmstadt, tuerk@gsc.tu-darmstadt.de, http://www.graduate-school-ce.de
[2] Institute of Numerical Methods in Mechanical Engineering, TU Darmstadt, Dolivostraße 15, 64293 Darmstadt
[3] Institute of Aerodynamics and Fluid Mechanics, TU Darmstadt, Alarich-Weiss-Str. 10, 64287 Darmstadt

**Key words:** Fluid-Structure Interaction, Aerodynamics, Flow Control

**Abstract.** In the present work, an airfoil with self adaptive camber is investigated. The camber is passively adapted to the flow by a kinematic coupling between the leading and trailing edge. For validation, the rigid NACA $64_3618$ airfoil is simulated at different angles of attack. Additional simulations are performed for a prescribed deflection at the leading and trailing edge with a qualitatively good agreement to experimental data. Conducting a series of fully coupled FSI simulations, a reduction in the lift coefficient of 44 % compared to the rigid airfoil could be achieved. The results from the CFD are compared to those of an inviscid panel method, where a deviation of approximately 10 % in the mean lift coefficient for the FSI scenario is observed.

## 1 INTRODUCTION

Despite the fact that the computational resources have been constantly growing for the last decades, the simulation of complex fluid dynamics problems such as the simulation of turbulence by using Direct Numerical Simulations (DNS) or also Large-Eddy Simulation (LES) is still limited to either simple geometries or moderate Reynolds numbers. Thus, RANS (Reynolds Averaged Navier Stokes) models are still the preferred method in industrial applications for pratically relevant Reynolds numbers. If URANS Methods are applied to typical unsteady problems such as the flow around a square cylinder, the results achieved by using RANS Models are quite satisfactory [3]. On the contrary, running simulations for naturally unsteady problems as a steady-state problem, the results are quite different.
This clearly illustrates the potential of using RANS models for the simulation of Fluid-Structure Interaction (FSI) problems. Those multiphysics simulations are unsteady in

general due to the interaction between the different physics. The main aspects of not statistically stationary flows can be captured by URANS if the time and length scales of the coherent structures are much larger than the scales of turbulence resulting in a separation of scales in the energy spectrum. For a rather slow structural motion, these conditions are fulfilled. Usually a few vortex sheddings are sufficient to obtain qualitatively good phase-averaged results with RANS simulations. By reducing the integration time, the overall computational cost is also reduced. Additionally, the requirements for the mesh resolution in streamwise and spanwise directions are less demanding than for all turbulence resolving methods.
The main objective of this work is to validate the use of URANS for the flow around a NACA $64_3618$ airfoil with self-adapting camber as proposed by Lambie [5]. For small angles of attack (AoA), in this case $\alpha < 5°$, the airfoil is not fully stalled and a good agreement between the numerical data and the experimental ones can be expected. Throughout this work, the $k-\omega-SST$ model from Menter [6] is used since it is well known for its good predictions in the field of aerodynamics problems. The results for a rigid airfoil at different angle of attack are compared to experimental data as well as the ones for a flexible leading and trailing edge with a fixed deflection angle. Additionally, a series of FSI simulations for a fully coupled system are performed to evaluate the effect of grid resolution, time step size and order of discretization on the mean lift coefficient.

## 2 GOVERNING EQUATIONS

In the following an incompressible fluid with constant fluid properties is considered. For an incompressible Newtonian fluid, the flow has to satisfy the continuity and Navier-Stokes equations in the following form:

$$\frac{\partial u_i}{\partial x_i} = 0 \quad , \tag{1}$$

$$\rho \frac{Du_i}{Dt} = -\frac{\partial p}{\partial x_i} + \mu \frac{\partial^2 u_i}{\partial x_j^2} \quad . \tag{2}$$

where $u_i$ is the velocity vector, $p$ is the static pressure and $\mu$ is the dynamic viscosity. Using the Reynolds decomposition,

$$u(\mathbf{x},t) = \overline{u(\mathbf{x})} + u'(\mathbf{x},t) \quad , \tag{3}$$

where $\overline{u}$ is the mean motion and $u'$ is the fluctuating component, the RANS equations can be derived from equation (2):

$$\frac{\partial \overline{u_i}}{\partial x_i} = 0 \quad , \tag{4}$$

$$\rho \frac{D\overline{u_i}}{Dt} = -\frac{\partial \overline{p}}{\partial x_i} + \mu \frac{\partial^2 \overline{u_i}}{\partial x_j^2} - \rho \frac{\partial \overline{u_i' u_j'}}{\partial x_j} \quad . \tag{5}$$

Thus, equation (5) is the ensemble average of equation (2), where an additional term arises. This additional term describes the momentum transport due to turbulence motion causing a closure problem.

## 3 NUMERICAL METHODS

In the present work, we are performing numerical simulations using the finite volume flow solver FASTEST [10] with block structured, boundary fitted grids. The convective fluxes are approximated with the first order UDS or second order GAMMA scheme [4]. For the time discretization, we use a backward differencing scheme with second order accuracy and the coupling between pressure and velocity is done with the SIMPLE algorithm. The parallelization in FASTEST is done via domain decomposition using MPI. For turbulence modelling, the $k-\omega-SST$ model from Menter [6] is used. For acceleration, a geometric multigrid is applied to the momentum equations and in the case of fluid-structure coupling, an implicit partitioned approach is used. To account for the mesh motion, the ALE formulation of eq. 4 and eq. 5 is applied. For the mesh generation, a transfinite interpolation [2] and an elliptic method [8] is used.

## 4 STRUCTURAL MODEL AND TESTCASE DESCRIPTION

In order to describe the structural motion of the airfoil, the model from Lambie [5] is used. This model allows for heaving, pitching and flap motion, whereas the leading and trailing edge are kinematically coupled. The Lambie-type airfoil will be described as a two-dimensional multibody system, shown in figure 1. The structural model includes the three degrees of freedom mention afore with the rotational axis for the leading and trailing edge and the main body located at (0.2/0.02453), (0.7/0.02946) and (0.3/0.0) respectively in the airfoil's local reference frame. The coupling factor for the kinematic coupling between the leading and trailing edge is set to $n = 3$. The resulting nonlinear differential equations are given in the APPENDIX.

The aerodynamic forces, shown in figure 1, are calculated within the flow solver FASTEST and sent to the structural model. After solving the equations of motion by a fourth order Runge Kutta method, the resulting displacements are sent back to FASTEST causing the motion of the boundary points and the remeshing. This iterative process is repeated until the equilibrium within the time step between fluid and structure is reached. For the fluid mesh, the first grid point in wall normal direction is located at $y^+ < 2$ for the entire airfoil as suggested in [5]. The final C-type mesh for all computations shown in this work consists of 70500 CVs, whereas the airfoil is discretized by 110 CVs in circumferential direction. No-slip boundary conditions are applied on the airfoil, symmetry boundary conditions are used in spanwise direction and typical inlet and outlet boundary conditions are employed. To enable the deflection of the leading and trailing edge, the edges of the red highlighted surfaces in figure 2 are regenerated using a cubic spline to

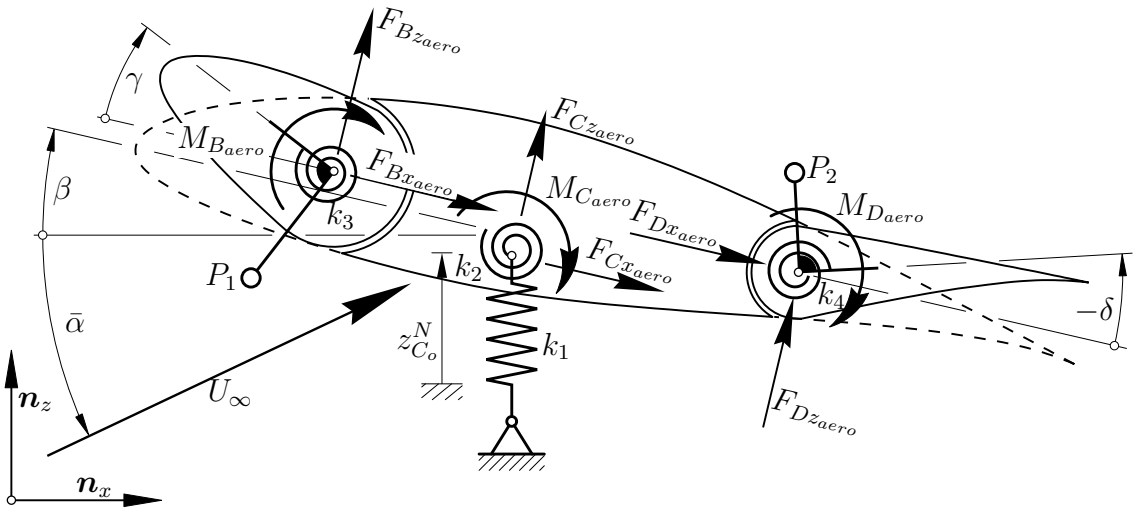


**Figure 1**: Discrete forces on the Lambie-type airfoil

avoid any discontinuities in the surfaces wrapped around the airfoil. Thus, a gap between the three different bodies can be avoided and preventing numerical problems related to such a gap.

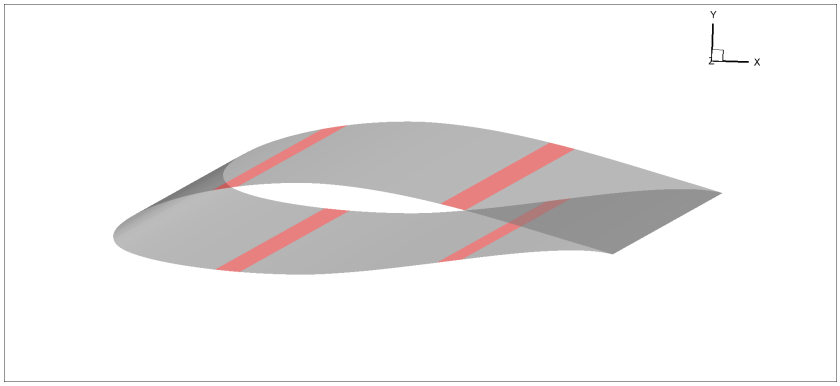

**Figure 2**: Surface representation of NACA $64_3618$ airfoil with deformable surfaces highlighted in red

## 5 RESULTS AND DISCUSSION

### 5.1 VALIDATION

In order to demonstrate the behaviour of the chosen RANS turbuluence model, the flow around a rigid NACA $64_3618$ airfoil at $Re = 1.36 \times 10^6$ for different AoA is simulated. The results, presented in figure 3, are in good agreement to the measurements from Abott [1] although the Reynolds number is about twice as big. The Reynolds number affects only the $c_{L,max}$ value which might be slighly lower for our Reynolds number. For zero angle of

attack, the results for $c_L$ deviate less than 1 %. The largest deviation can be found for high AoA, where the airfoil is fully stalled. The deviations at large AoA (stall) are related to the assumption of isotropic turbulence in the RANS approach which is clearly violated in case of separated flows. It is also found that the chosen grid resolution is sufficient for small AoA ($\alpha < 5°$), but has to be increased as the angle of attack increases. For all simulations, the GAMMA scheme was used.

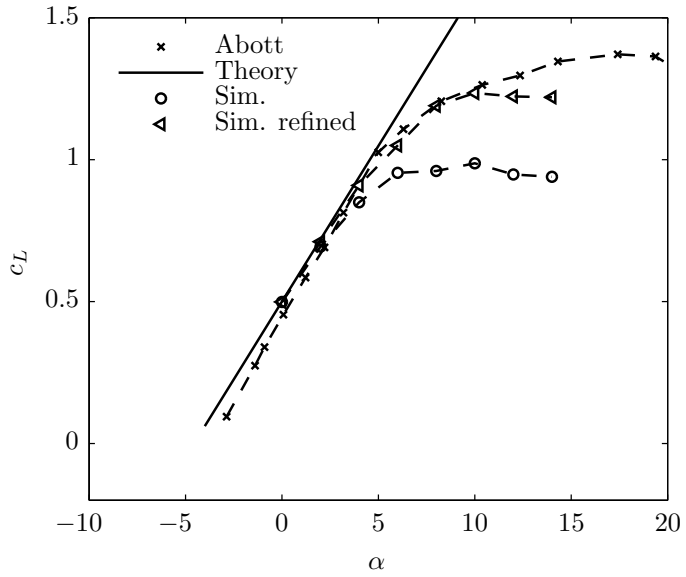


**Figure 3**: Rigid airfoil: lift Coefficient versus angle of attack $\alpha$, $Re = 1.36 \times 10^6$

Additional simulations for a fixed flap configuration, $\gamma = -5°$ (leading edge) and $\delta = -10°$ (trailing edge), were conducted from $\alpha = 0°$ to $\alpha = 10°$. The flow around the deflected leading and trailing edge is separated for all $\alpha$ investigated in this work. For $\alpha = 0°$, the resulting flow field is illustrated in figure 4, where the separation at the trailing edge can be clearly detected. Again, a strong grid dependency can be found for large values of $\alpha$. The second order upwind scheme is applied in all simulations. In comparison to the experiment, a very similiar trend for the slope can be found: the deflection of the leading edge reduces the slope from the theoretical value of $\partial c_L/\partial\alpha = 2\pi$. The increase in the lift coefficient is directly related to the geometrical changes at the trailing edge. Due to the presence of three dimensional effects within the experiment, the experimental results are corrected according to the empirical formula from Betz [7] which is suggested by Lambie [5]. The simulated curve is in between the measured and corrected experimental values. In the simulations the deflected airfoil is fully stalled at $\alpha \approx 5°$, whereas in the experiments the stall angle is at $\alpha \approx 8°$ for the corrected case and about $\alpha \approx 13°$ for the uncorrected one. Based on the results presented, we will focus on small angles of attack for the following coupled fluid-structure interaction simulations.

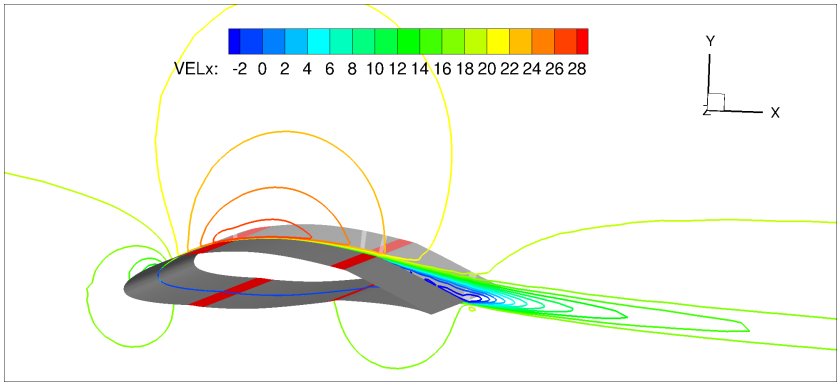


**Figure 4**: Isolines of streamwise velocity for $\gamma = -5°$ (leading edge) and $\delta = -10°$ (trailing edge), deformable surfaces highlighted in red

## 5.2 FLUID-STRUCTURE INTERACTION

For the fully coupled simulation, the structural parameters are set to the ones used by Lambie [5] for the enhanced model. The torsional spring stiffness $k_\gamma$ is set to 500 Nm/rad. Within this study, the simulations presented in table 1 have been performed in order to investigate the effect of different grid spacings, time step sizes and discretization orders on the mean lift coefficient at the final equilibrium. Additionally, the aerodynamic forces and moments as well as the final displacements are compared to simulation conducted with an inviscid panel method. The results for the lift coeffcient are given in table 1. All simulations were run for at least 10 seconds in physical time to ensure that the state of equilibrium was reached (see figure 6), whereas the computational time step was $\Delta t = 2 \times 10^{-4}$.

**Table 1**: Overview of the simulations performed and resulting mean lift coefficient at equilibrium

| | Grid spacing | Time step size | scheme | $c_L$ |
|---|---|---|---|---|
| case 1 | 2h | $2\Delta t$ | UDS | 0.28 |
| case 2 | h | $2\Delta t$ | UDS | 0.29 |
| case 3 | 2h | $\Delta t$ | UDS | 0.28 |
| case 4 | 2h | $2\Delta t$ | GAMMA | 0.29 |
| panel [9] | - | - | - | 0.32 |

The results in table 1 indicate that the results for the mean lift coefficient are hardly affected by refining the grid or the time step, or the discretization method. The lift coefficient obtained from an inviscid panel code is about 10% higher than in the CFD case. However, the results for the equations of motion are in very good agreement as it is shown for the pitching motion in figure 6. For the remaining degrees of freedom, the

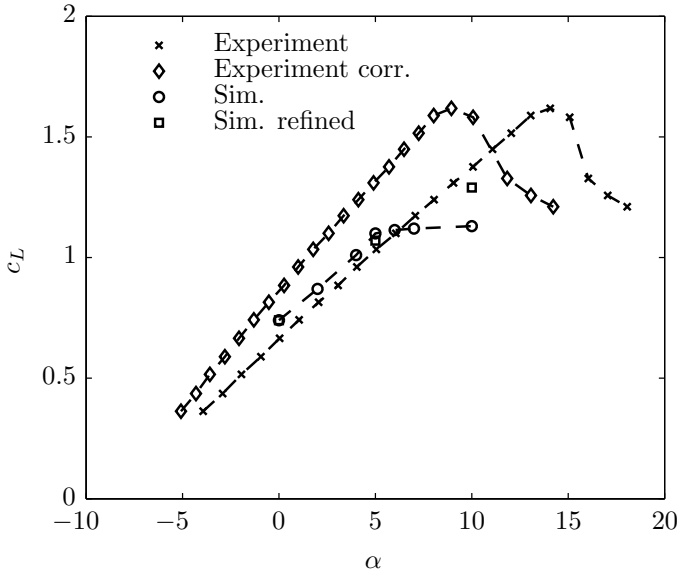


**Figure 5**: Lift Coefficient versus angle of attack $\alpha$, $Re = 1.36 \times 10^6$ for $\gamma = -5°$ and $\delta = -10°$

deviation is always less than 10 %. The largest difference occurs for the aerodynamic moment on the leading edge. Whereas a positiv moment is predicted by the panel code, a negative value is calculated in the CFD and thus, mainly causing the difference in the lift coefficient. Note that for an inviscid panel method, drag forces cannot be calculated. Since the negative rotational angle at the leading edge causes an increase in drag, this effect also influences the overall results but is not captured within the panel code. Additionally, the deformation of the airfoil is handled differently such that the deformed airfoil differs in the red highlighted sections shown in figure 2. Comparing the results obtained for the fully coupled simulation of a flexible airfoil to those of a rigid airfoil, the mean lift coefficient could be reduced by approximately 44%. Thus, the potential of the Lambie-type airfoil could also be demonstrated numerically. A direct comparison to experimental data is not possible here, since the experimental setup did not allow for heaving and pitching.

## 6 CONCLUSION

A series of computations for a rigid airfoil, a flexible airfoil with prescribed deflections and fully coupled FSI simulations have been performed. For the rigid airfoil, the mesh resolution has been investigated. The resolution has to be increased as the angle of attack increases. However, for small angles of attack, $\alpha < 5°$, the results were in good agreement to experimental data. A qualitatively good agreement could also been found for the flexible airfoil for $\gamma = -5°$ (leading edge) and $\delta = -10°$ (trailing edge). In the fully coupled FSI simulations a reduction in the mean lift coefficient of 44 % for the flexible airfoil compared to the rigid one could be achieved. The results from the CFD showed a

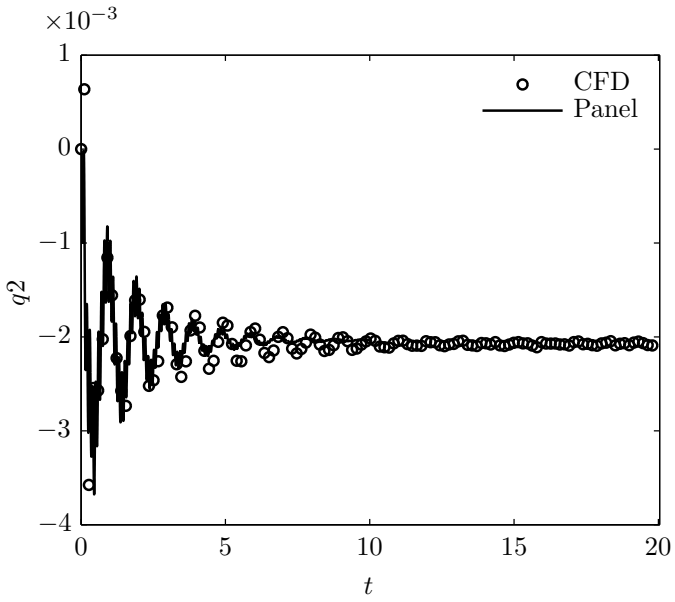


**Figure 6**: Time history of pitch angle for CFD simulations and panel method

difference of about 10 % to an inviscid panel method. In the future, the simulations will be repeated by using hybrid RANS/LES turbulence models to account for the anisotropic effects arising from the separation.

## AFFILIATION

This work is supported by the 'Excellence Initiative' of the German Federal and State Governments and the Graduate School of Computational Engineering at Technische Universität Darmstadt.

## REFERENCES

[1] I. H. Abbott. *Theory of Wing Sections, Including a Summary of Airfoil Data*. Courier Dover Publications, 1959.

[2] W. J. Gordon and C. A. Hall. Construction of curvilinear co-ordinate systems and applications to mesh generation. *International Journal for Numerical Methods in Engineering*, 7(4):461477, 1973.

[3] G. Iaccarino, A. Ooi, P. A. Durbin, and M. Behnia. Reynolds averaged simulation of unsteady separated flow. *International Journal of Heat and Fluid Flow*, 24(2):147–156, April 2003.

[4] H. Jasak, H. Weller, and A. Gosman. High resolution NVD differencing scheme for arbitrarily unstructured meshes. *International Journal for Numerical Methods in Fluids*, 31(2):431449, 1999.

[5] B. Lambie. *Aeroelastic Investigation of a Wind Turbine Airfoil with Self-Adaptive Camber*. Ph.D. thesis, TU Darmstadt, April 2011.

[6] F. R. Menter. Zonal two equation kappa-omega turbulence models for aerodynamic flows. *c1993*, -1, 1993.

[7] L. Prandtl. *Ergebnisse der Aerodynamischen Versuchsanstalt zu Göttingen*. Universitätsverlag Göttingen, 2009.

[8] S. P. Spekreijse. Elliptic grid generation based on laplace equations and algebraic transformations. *Journal of Computational Physics*, 118(1):38–61, April 1995.

[9] H. Spiegelberg, U. Cordes, P. Hagedorn, and C. Tropea. Note on a self-adaptive airfoil with kinematically coupled leading and trailing flap. In Horst Ecker, Alois Steindl, and Stefan Jakubek, editors, *ENOC 2014 - Proceedings of 8th European Nonlinear Dynamics Conference*. Institute of Mechanics and Mechatronics, Vienna University of Technology, 2014. ISBN: 978-3-200-03433-4.

[10] D. C. Sternel. FASTEST-Manual, 2005.

## APPENDIX

For the discrete forces on the Lambie-type airfoil, presented in figure 1, and its corresponding topolgy in figure 7, the resulting nonlinearized equations of motion are given in [9] as follows:

$$
\begin{aligned}
&m_A\ddot{q}_1 + d_1\dot{q}_1 + k_1 q_1 \\
&-\ddot{q}_2(S_{Cx}\cos q_2 + S_{Cz}\sin q_2) \\
&+\dot{q}_2^2(S_{Cx}\sin q_2 - S_{Cz}\cos q_2) \\
&+(\dot{q}_2+\dot{q}_3)^2\big(S_{Bx}\sin(q_2+q_3) - S_{Bz}\cos(q_2+q_3)\big) \\
&-(\ddot{q}_2+\ddot{q}_3)\big(S_{Bx}\cos(q_2+q_3) + S_{Bz}\sin(q_2+q_3)\big) \\
&-\big(n\ddot{q}_3 + n'\dot{q}_3^2 + \ddot{q}_2\big)\big(S_{Dx}\cos(q_2+\delta) + S_{Dz}\sin(q_2+\delta)\big) + \\
&\quad + (n\dot{q}_3+\dot{q}_2)^2\big(S_{Dx}\sin(q_2+\delta) - S_{Dz}\cos(q_2+\delta)\big) \\
&= F_{Az_{aero}}\cos q_2 - F_{Ax_{aero}}\sin q_2
\end{aligned}
\tag{6a}
$$

$$
\begin{aligned}
&\Theta_A^{(C_o)}\ddot{q}_2 + d_2\dot{q}_2 + k_2 q_2 + \ddot{q}_3(\Theta_B^{(B_o)} + n\Theta_D^{(D_o)}) + n'\Theta_D^{(D_o)}\dot{q}_3^2 \\
&-\ddot{q}_1\ (S_{Cx}\cos q_2 + S_{Cz}\sin q_2 \\
&\quad + S_{Dx}\cos(q_2+\delta) + S_{Dz}\sin(q_2+\delta) + S_{Bx}\cos(q_2+q_3) + S_{Bz}\sin(q_2+q_3)) \\
&-(2\dot{q}_2\dot{q}_3 + \dot{q}_3^2)\big(S_{Bx}(x_{B_o}^C\sin q_3 + z_{B_o}^C\cos q_3) - S_{Bz}(x_{B_o}^C\cos q_3 - z_{B_o}^C\sin q_3)\big) \\
&+(2\ddot{q}_2+\ddot{q}_3)\big(S_{Bx}(x_{B_o}^C\cos q_3 - z_{B_o}^C\sin q_3) + S_{Bz}(x_{B_o}^C\sin q_3 + z_{B_o}^C\cos q_3)\big) \\
&-(n^2\dot{q}_3^2 + 2n\dot{q}_2\dot{q}_3)\big(S_{Dx}(x_{D_o}^C\sin\delta + z_{D_o}^C\cos\delta) - S_{Dz}(x_{D_o}^C\cos\delta - z_{D_o}^C\sin\delta)\big) \\
&+(n\ddot{q}_3 + n'\dot{q}_3^2 + 2\ddot{q}_2)\big(S_{Dx}(x_{D_o}^C\cos\delta - z_{D_o}^C\sin\delta) + S_{Dz}(x_{D_o}^C\sin\delta + z_{D_o}^C\cos\delta)\big) \\
&= M_{A_{aero}}
\end{aligned}
\tag{6b}
$$

$$
\begin{aligned}
&\ddot{q}_3(\Theta_B^{(B_o)} + n^2\Theta_D^{(D_o)}) + \dot{q}_3\left(d_3 + d_4 n^2\right) + k_3 q_3 \\
&+k_4 n\delta(q_3) + nn'\Theta_D^{(D_o)}\dot{q}_3^2 + M_{spr}(q_3) \\
&-\ddot{q}_1\ (+S_{Bx}\cos(q_2+q_3) + S_{Bz}\sin(q_2+q_3) \\
&\quad + S_{Dx}n\cos(q_2+\delta) + S_{Dz}n\sin(q_2+\delta)) \\
&+\ddot{q}_2\ (n\Theta_D^{(D_o)} + \Theta_B^{(B_o)} \\
&\quad + S_{Bx}(x_{B_o}^C\cos q_3 - z_{B_o}^C\sin q_3) + S_{Bz}(x_{B_o}^C\sin q_3 + z_{B_o}^C\cos q_3) \\
&\quad + S_{Dx}n(x_{D_o}^C\cos\delta - z_{D_o}^C\sin\delta) + S_{Dz}n(x_{D_o}^C\sin\delta + z_{D_o}^C\cos\delta)) \\
&+\dot{q}_2^2\ (S_{Bx}(x_{B_o}^C\sin q_3 + z_{B_o}^C\cos q_3) - S_{Bz}(x_{B_o}^C\cos q_3 - z_{B_o}^C\sin q_3) \\
&\quad + S_{Dx}n(x_{D_o}^C\sin\delta + z_{D_o}^C\cos\delta) - S_{Dz}n(x_{D_o}^C\cos\delta - z_{D_o}^C\sin\delta)) \\
&+M_{spr}(q_3) \\
&\quad = M_{B_{aero}} + nM_{D_{aero}}
\end{aligned}
\tag{6c}
$$

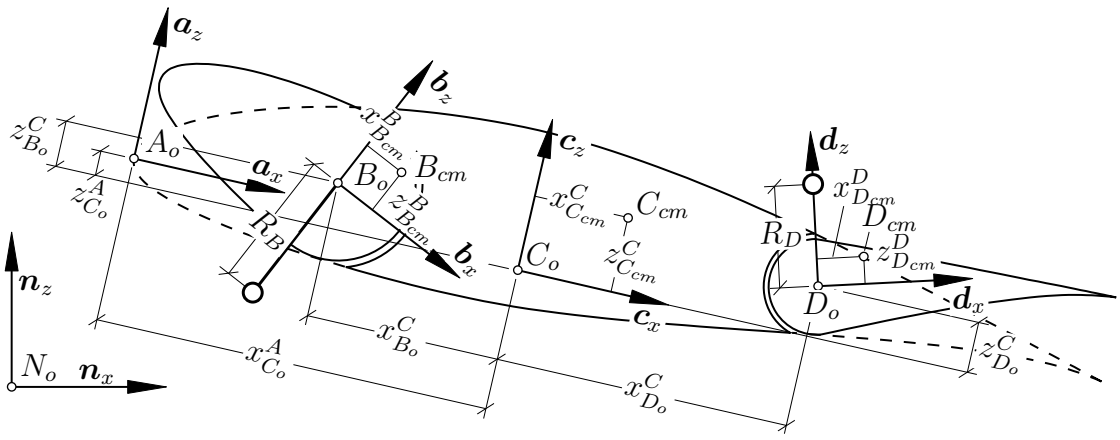


**Figure 7**: Topology of the Lambie-type airfoil

In order to simplify the equations some general terms have been defined

$$\Theta_C^{(C_o)} = \Theta_C^{(C_{cm})} + m_C((x_{C_{cm}}^C)^2 + (z_{C_{cm}}^C)^2), \tag{7}$$

$$\Theta_B^{(B_o)} = \Theta_B^{(B_{cm})} + m_B((x_{B_{cm}}^B)^2 + (z_{B_{cm}}^B)^2), \tag{8}$$

$$\Theta_D^{(D_o)} = \Theta_D^{(D_{cm})} + m_D((x_{D_{cm}}^D)^2 + (z_{D_{cm}}^D)^2), \tag{9}$$

$$\begin{aligned}\Theta_A^{(C_o)} = \ & \Theta_C^{(C_o)} + \Theta_B^{(B_o)} + \Theta_D^{(D_o)} \\ & + m_B((x_{B_o}^C)^2 + (z_{B_o}^C)^2) + m_D((x_{D_o}^C)^2 + (z_{D_o}^C)^2)\end{aligned} \tag{10}$$

$$m_A = m_B + m_C + m_D \tag{11}$$

$$S_{Bx} = m_B x_{B_{cm}}^B \tag{12}$$

$$S_{Bz} = m_B z_{B_{cm}}^B \tag{13}$$

$$S_{Cx} = m_C x_{C_{cm}}^C + m_B x_{B_o}^C + m_D x_{D_o}^C \tag{14}$$

$$S_{Cz} = m_C z_{C_{cm}}^C + m_B z_{B_o}^C + m_D z_{D_o}^C \tag{15}$$

$$S_{Dx} = m_D x_{D_{cm}}^D \tag{16}$$

$$S_{Dz} = m_D z_{D_{cm}}^D \tag{17}$$

$$F_{Ax_{aero}} = F_{Bx_{aero}} + F_{Cx_{aero}} + F_{Dx_{aero}} \tag{18}$$

$$F_{Ax_{aero}} = F_{Bz_{aero}} + F_{Cz_{aero}} + F_{Dz_{aero}} \tag{19}$$

$$\begin{aligned}M_{A_{aero}} = \ & M_{B_{aero}} + M_{C_{aero}} + M_{D_{aero}} \\ & - x_{B_o}^C F_{Bz_{aero}} + z_{B_o}^C F_{Bx_{aero}} - x_{D_o}^C F_{Dz_{aero}} + z_{D_o}^C F_{Dx_{aero}}\end{aligned} \tag{20}$$